Heliyon 5 (2019) e02695

Contents lists available at ScienceDirect

Heliyon

journal homepage: www.heliyon.com

Heliyon

Research article

# Analysis of crystallization fouling in electric water heating

Alexander Janzen [a,*], Eugeny Y. Kenig [b,c]

[a] Stiebel Eltron GmbH & Co. KG, Dr.-Stiebel-Straße 33, Holzminden, 37603, Germany
[b] Chair of Fluid Process Engineering, University of Paderborn, Pohlweg 55, Paderborn, 33098, Germany
[c] Gubkin Russian State University of Oil and Gas, Moscow, Russian Federation

ARTICLE INFO

*Keywords:*
Chemical engineering
Electrical engineering
Electrochemistry
Electric water heating
Influencing factors
Crystallization fouling
Electrical leakage current

ABSTRACT

In the present study, the main influencing factors of crystallization fouling in electric water heating were investigated. Dependence on the saturation index and four operating parameters was analyzed, namely: liquid temperature, surface temperature, flow rate and electrical leakage current. A focus of the study was the influence of electrical leakage current on the fouling behavior and the morphology of the deposited crystal layers. The investigation shows that the aforementioned parameters influence the fouling process and crystal size growth in a different way. The experimental results were used to find a correlation between the electrical leakage current and induction time. In addition, a modeling approach is presented which allows an estimation of the fouling mass flux.

## 1. Introduction

### 1.1. Electric water heating

The electric water heating industry covers a wide range of applications, e.g. tankless water heaters, hot water storage tanks and drinking water heat pumps. All these domestic appliances contain electric heating elements. Many conventional heating elements for electric water heating are based on either a tubular or a bare-wire heating system. There also exist some other new approaches to heating elements, e.g. infrared heating elements [1] or ceramic heating elements [2], but up to now they have not been able to force way through electric water heating.

A tubular heating element is an electric resistance heater in a sheath made of copper, stainless steel or steel. A heating wire is embedded inside the metal tube and electrically insulated in highly compressed magnesium oxide. The heating fluid has no contact with the heating wire. Due to the poor thermal conductivity of magnesium oxide, the surface temperature of the heating wire increases. Since it is highly susceptible to crystalline deposits, its lifetime is also limited. Tubular heating elements are not affected by air dissolved in the water and are suitable for soft water conditions [3, 4].

Bare wire heating elements on the other hand are placed directly in the circulating fluid. Therefore, they need a completely different kind of electrical insulation. The heating elements are placed into a pressure-tested insulated block. Insulation resistance is ensured by long and narrow channels before and behind electric heating elements. The resistance depends on the properties of the fluid flowing through the channels and by the channel geometry. Accordingly, the electrical resistance and conductivity of the fluid are important for the operating conditions. Bare wire heating elements are especially suitable for use in hard water conditions, because they have a low mass and a large surface compared to tubular heating elements [5].

According to Gusig and Schmitz [5], conventional electric heating systems have advantages and disadvantages, which are summarized in Table 1.

The properties of electric heating elements result in different types of fouling behavior, which justify a closer investigation.

### 1.2. Crystallization fouling

Contamination of water heating equipment is a general problem for electric water heating industry. Especially, crystallization fouling is the undesired deposition of crystals on heat transfer surfaces, which can cause severe damage to the heat exchanger, as discussed by Müller-Steinhagen [6]. According to several investigations [7, 8, 9, 10, 11, 12, 13], fouling can occur on any fluid-solid surface and cause additional negative effects, e.g. increased pressure loss.

Deposition of calcium carbonate scale is frequently encountered in electric water heating operations. Calcium carbonate has three polymorphs: calcite, aragonite and vaterite. Since calcite and aragonite are the most stable crystalline forms of calcium carbonate, they are much more common in tap water heating as other crystal forms. Deposition of

* Corresponding author.
*E-mail address:* alexander.janzen@stiebel-eltron.de (A. Janzen).

https://doi.org/10.1016/j.heliyon.2019.e02695
Received 29 December 2018; Received in revised form 1 September 2019; Accepted 16 October 2019

**Table 1**
Advantages and disadvantages of heating systems.

| Bare wire heating systems | Tubular heating systems |
|---|---|
| **Advantages** | |
| low surface temperature | no electrical contact with the fluid |
| fast cooling because of low thermal mass | low pressure loss |
| **Disadvantages** | |
| direct electrical contact with the fluid | high surface temperature |
| high pressure loss because of long and narrow channels | slow cooling because of high thermal mass |

$CaCO_3$ scale results from precipitation of calcium carbonate according to the following equation:

$$Ca^{2+} + CO_3^{-2} \rightarrow CaCO_3 \tag{1}$$

Moreover, calcium carbonate scale can also be formed by combination of calcium and bicarbonate ions, as explained in [8].

To characterize the thermal performance of heat transfer surfaces which are subject to fouling, the overall heat transfer coefficient $k$ for the heat exchanging fluid has been defined according to Eq. (2), in which α is the heat transfer coefficient, $x_{1,f}$ and $x_{2,f}$ are the fouling thickness on inner and outer wall sides, $x_w$ is the thickness of the wall and λ is the thermal conductivity.

$$\frac{1}{k_f} = \frac{1}{\alpha_{1,f}} + \frac{x_{1,f}}{\lambda_{1,f}} + \frac{x_w}{\lambda_w} + \frac{x_{2,f}}{\lambda_{2,f}} + \frac{1}{\alpha_{2,f}} \tag{2}$$

On the other hand, the overall heat transfer coefficient $k$ is calculated based on the temperature difference between the heating element surface $T_{HZP}$ and the fluid $T_{fl}$. Furthermore, the heat flux $\dot{q}_{el,f}$ at the heating element is used as follows:

$$k_f = \frac{\dot{q}_{el,f}}{T_{HZP} - T_{fl}} \tag{3}$$

If fouling occurs on one side only and if all operating parameters of the heat exchanging fluid are maintained constant, the fouling resistance $R_f$ may be determined by

$$R_f = \frac{1}{k_f} - \frac{1}{k_0} \tag{4}$$

where $k_f$ is the overall heat transfer coefficient for the fouling case and $k_0$ is the overall heat transfer coefficient for the initial clean condition.

The following equation expresses the dependence of the fouling resistance on the temporally changing fouling mass flux:

$$\frac{dR_f}{dt} = \frac{1}{\lambda_f \cdot \rho_f} \cdot J_f \tag{5}$$

The fouling mass flux $J_f$ is estimated by taking the difference of two opposing factors, a deposit term $J_{i,D}$ and a removal term $J_r$, as follows:

$$J_f = J_{i,D} - J_r \tag{6}$$

Fig. 1 shows a typical fouling curve, as discussed by Förster [10]. The characteristic fouling process is subdivided into two successive fouling stages: the induction period and the layer growth period. The induction period is further separated into initialization phase ($A_1$) and roughness-controlled phase ($A_2$). The induction period is described by the initialization time, turn point time and induction time. An induction period is visible in many, yet not in all cases. Its occurrence is primarily determined by molecular and mechanical interactions at the interface between the crystalline deposits and the heat transfer surface. In most cases, no degradation of the heat transfer is observed during this period. The initialization time describes the begin of the first nucleation and crystal growth. After this time, the heat transfer coefficient increases more strongly than the heat conduction resistance. The turn point time corresponds to the maximum heat transfer coefficient. After this time, the heat transfer coefficient slowly decreases, and the heat conduction resistance continuously increases. The induction time determines the end of the induction period. This is followed by the layer growth period, which is accompanied by a reduction in the heat transfer coefficient. The temporal evolution of the fouling process may take various forms. A distinction is made between exponential, linear, continuously increasing, asymptotic and saw tooth behavior.

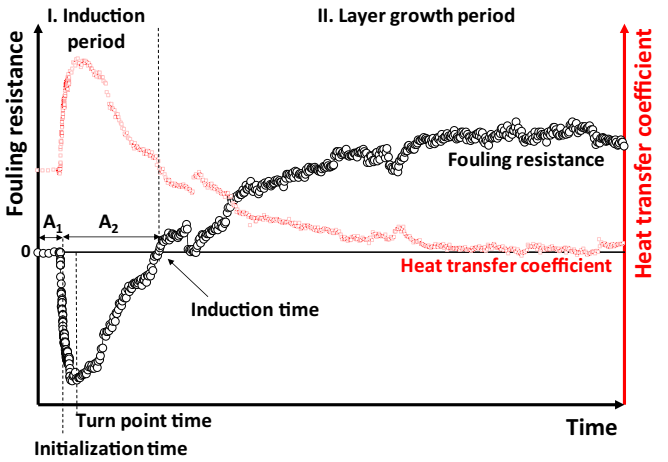


**Fig. 1.** A characteristic fouling curve for a $CaCO_3$ solution, $A_1$: Initialization phase, $A_2$: Roughness-controlled phase (our own measurements).

To evaluate a saturated system, the products of a performed tap water analysis are summarized in the ionic activity product $IAP$. The ratio of the $IAP$ to the equilibrium solubility product $K_L$, as reported by Wisotzky [14] for various salts, is a measure of the saturation state and is called degree of saturation. Usually, however, the saturation index according to Eq. (7) is used, which is the logarithm of this ratio.

$$SI = \log\left(\frac{IAP}{K_L}\right) \tag{7}$$

For a supersaturation of the solution, the saturation index must be greater than zero. The saturation index is used as a measure of the saturation state of a multicomponent test fluid.

### 1.3. Electrochemical issues

When a metal is in contact with an electrolytic solution, a potential difference builds up between the two phases. This natural potential difference $\Delta\varphi_{DC,N}$, which is characterized by the electrochemical double layer and operating parameters, is called zeta potential. It is an energetic surface property and a function of the electrolyte. In the so-called electrolyte-free water, the charged metal is surrounded by a cloud of ions of predominantly opposite charge. According to Erdey-Grúz [15], the surface charges compensate the metallic charges in the water, so that it appears macroscopically neutral to the outside. Actually, several ionic layers are formed in electrolyte-containing media. First, the so-called inner Helmholtz layer forms. This inner layer is characterized by dehydrated ions and dipoles. Subsequently, a second layer is deposited on the dehydrated ions with opposite charges. This layer is referred to as the outer Helmholtz layer. Due to the hydration shell in the outer Helmholtz layer, the ions occupy a larger space than the dehydrated ions in the inner Helmholtz layer. Therefore, the surface charge cannot be completely compensated and a diffuse layer of different charged ions is formed around the metal, as illustrated in Fig. 2.

The thickness of the diffuse layer is determined by the charge balancing. Hence, the electrical potential drop in the entire double layer consists of two potential differences in the Helmholtz layers and the diffuse layer. The ions in the fluid can be adsorbed on the metallic surface when they interact with the metal through van der Waals mechanism, or

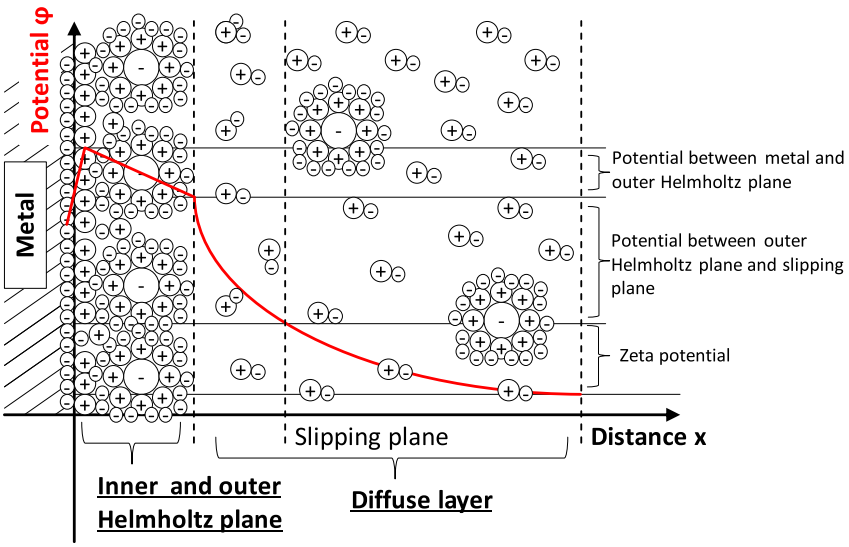


**Fig. 2.** Principle illustration of the electrochemical double layer [16].

when a Coulomb interaction between the solution components and the surface is established. The adsorption of the ions is supported, weakened or inhibited depending on the potential differences between the metallic surface and the solution components. According to Hamann and Vielstich [16], anions are particularly prone to the so-called specific adsorption. Due to van der Waals forces, anions can, therefore, adsorption on a surface even if the metallic surface has negative excess charges.

When an external DC voltage is applied between the metal of the heating element and an opposing electrode, the potential $\varphi_{Me}$ of the metallic surface is changed by polarization. This change also affects the electrical potential difference $\Delta\varphi_{DC,E}$ across the double layer. Due to the applied DC voltage, the ions in the fluid are accelerated to the metal or to the opposing electrode. This results in an induced dipole effect and a decrease or increase of the diffuse layer thickness. According to Erdey-Grúz [15] and Vetter [17], there is no polarization of the electrode when an external AC voltage is applied. However, the AC voltage and the resulting electrical current flow change the potential difference $\Delta\varphi_{AC,E}$ over time. The AC voltage leads to a local charge reversal of the double layers with the frequency of the AC voltage. As a result, the ion adsorption accelerated following the frequency at positively charged areas and slowed down at negatively charged areas or may be completely inhibited.

A further effect is considered to be important in the investigations. Over time, a formation of oxide layers can be observed on the metallic surface. According to Erdey-Grúz [15], in most cases, the formation of oxide layers begins with increasing anodic potential. The quantity depends on the material used and the superimposed potential. The latter may be in the form of a DC or AC voltage. Thus, the kinetics of the electrochemical oxygen evolution is largely dependent on the operating conditions, the chemical nature of the metal, the surface condition, and the quality of the adsorbed oxygen layer. Two special characteristics can be observed when applying an external AC voltage. First, anodic oxygen evolution takes place in the alternation of the frequency followed by a cathodic oxygen reduction. Second, depending on the direction of the electrical current, the cathodic oxygen reduction is stimulated by the alternating current and anodic oxygen evolution is favored. Which of the two procedures predominates during the experiments depends on the material used and the water composition. According to Rizzo [18], an oxidized heat transfer surface influences the induction time and the fouling process.

If electrical current flows in the tap water between two electrodes, it is possible that corrosion fouling occurs. In this work, two different metals (brass and stainless-steel) were used. Generally, brass corrosion occurs when the components of the brass alloy, such as zinc, copper, tin and lead, corrode as the result of the contact with water, as discussed by Sarver et al. [19]. Since brass typically contains a significant amount of zinc, it is susceptible to dezincification or to the corrosion of this zinc. Zinc will selectively corrode in the alloy, while only a weak shell consisting of the remaining copper remains. Corroded brass that has been dezincified can be identified by a splotchy reddish or pink coloring. Dezincification occurs only in high zinc alloys, especially yellow brass (67% Zn - 33% Cu). Generally, zinc is amphoteric and is attacked by hydroxyl ions:

$$Zn + 2\ OH^- + H_2O = Zn(OH)_2 + H_2O \tag{8}$$

Brass is also susceptible to other forms of corrosion caused by different chemicals, such as ammonia or mercury, that attack brass causing it to weaken.

Corrosion of steel can be considered as an electrochemical process that occurs in stages, as discussed in [20]. Initial attack occurs at anodic areas on the surface, where ferrous ions go into solution. Electrons are released from the anode and move through the metallic structure to the adjacent cathodic sites on the surface, where they interact with oxygen and water to form hydroxyl ions. The latter react with the ferrous ions from the anode to produce ferrous hydroxide, which itself is further oxidized in tap water to produce hydrated ferric oxide. These reactions can be represented by the following overall equation:

$$Fe + 3\ O_2 + 2\ H_2O = 2\ Fe_2O_3H_2O \tag{9}$$

The corrosion process requires simultaneous presence of water and oxygen. In the absence of either, corrosion does not occur.

### 1.4. Research objectives and conditions

The main objective of the present work is to show that the defined parameters have an impact on crystallization fouling in electric water heating.

In the first step, the following parameters were selected: (a) liquid temperature, (b) surface temperature, (c) flow rate, (d) electrical leakage current and (e) saturation index. The investigations were carried out independently of the geometry and surface properties of different heating elements. This means that geometry and surface properties of the heating elements are not considered. A cylindrical brass bolt and a stainless-steel bolt are operated as heated objects.

In contrast to other research works, as, e.g., [9, 10, 11], the fouling tests were carried out in a contaminated fluid. The characteristics of the

fluid that are typically found in the electric water heating industry are analyzed and described in Section 2.

## 2. Experimental

In many research studies, the parameters are analyzed in systems with only one dissolved salt type. Normally, the fluid consists of many different tap water components. These components are calcium, magnesium, sodium and potassium cations, which can react with existing anions, such as hydrogen carbonates, chlorides, sulfates and nitrates. The deposits are often formed based on inverse soluble complex compounds such as calcium carbonate and calcium sulfate. However, the presence of additional tap water components can influence the crystallization fouling through interaction effects. Therefore, the saturation indexes of the corresponding mineral phases in the test fluids are calculated with the commercial hydrogeochemical calculation program PHREEQC [21]. To determine the saturation index and the influence of the test fluid, a tap water sample was taken before and after each test, followed by tap water analysis. A total of 60 tap water analyses were evaluated and the arithmetic mean was used as a reference value for the different tap water components. The saturation index is calculated for the mineral phase $CaCO_3$ (aragonite). Table 2 illustrates the data obtained from the tap water analysis.

Two experimental set-ups were designed to study the characteristics of crystallization fouling. Set-up A (Fig. 4) was operated under neglect of flow conditions to confirm the influence of electrical leakage current on crystallization fouling and the morphology of the deposited crystal layers. The deposited crystals were analyzed with FT-IR-spectroscopy (Fourier transform infrared spectroscopy) to characterize what was really formed on the heating surface. The morphology of the deposited crystals on the bolt surfaces was analyzed with a light microscope depending on the leakage current. The light microscope images were also used to determine the crystal length and average hydraulic crystal diameter at each bolt using the program ImageJ. Some crystal length were measured on the soiled bolt surface as demonstrated in Fig. 3.

Subsequently, the average crystal length $L_{c,m}$ was calculated using the following equation:

$$L_{c,m} = \frac{\sum_i^n L_{c,i}}{n} \tag{10}$$

Here, $L_{c,i}$ is the unique crystal length of each measured crystal and $n$ is the number of measured crystals.

In a similar way, the average crystal diameter $d_{c,m}$ was calculated.

**Table 2**
Results of tap water analysis.

| Property/component | Unit | Value |
|---|---|---|
| Temperature | [°C] | 12.5 |
| pH value | [-] | 7.4 |
| Electrical conductivity | [μS/cm, 25 °C] | 897.4 |
| Oxygen | [mmol/l] | 0.1 |
| Total hardness | [°dH] | 29.2 |
| Carbonate hardness | [°dH] | 15.0 |
| Hydrogen carbonate | [mmol/l] | 5.4 |
| Chloride | [mmol/l] | 0.5 |
| Sulfate | [mmol/l] | 2.2 |
| Nitrate | [mmol/l] | 0.1 |
| Manganese | [mmol/l] | 0.0 |
| Iron | [mmol/l] | 0.002 |
| Copper | [mmol/l] | 0.001 |
| Calcium | [mmol/l] | 3.0 |
| Magnesium | [mmol/l] | 2.4 |
| Sodium | [mmol/l] | 0.2 |
| Potassium | [mmol/l] | 0.1 |
| SI Aragonite | [-] | 0.13 |
| SI Aragonite, $T_f = 60$ °C | [-] | 0.71 |
| Pressure | [hPa] | 1002.0 |

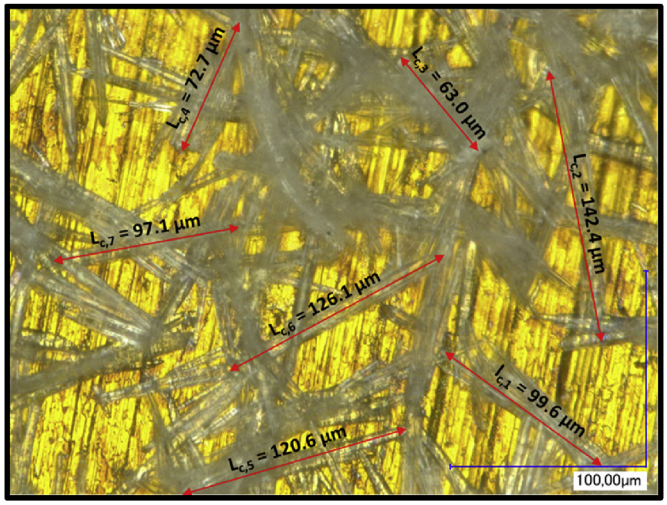


**Fig. 3.** Measurement of the local crystal length over the soiled brass bolt surface.

Furthermore, the contaminated heating surface was analyzed by X-ray fluorescence after the fouling tests. In this case, the bolt surfaces without crystals were studied. The crystals were removed from the surface to analyze the bolt surface. In experimental set-up A, brass and stainless-steel bolts were used.

Experimental set-up B (Fig. 5) was used for the investigations with continuous flow conditions to study the influence of operating parameters on the fouling resistance. In this set-up, only brass bolts were used as heated objects.

In all cases, each tank contained a brass or stainless-steel bolt supplied with appropriate holes for the implementation of maximum four high-efficiency electric heating cartridges (HS-654, Ø 6.5 × 40, 200 W, 230 V). Two temperature sensors were installed near the surface to determine the fouling resistance. The containers were equipped with electrodes to induce an alternating electrical potential in water. An alternating voltage with a frequency of 50 Hz was applied and an alternating electrical current occurred.

Table 3 gives the mean operating parameters of experimental set-up A.

Fig. 4 shows several fouling test tanks running in parallel and filled with 2.5 l of water. In addition to the measured thermal values, such as bolt surface temperature, water temperature and ambient temperature, the electrical voltage and electrical current were also recorded to determine the electrical power. A variable ratio transformer allowed precise adjustment of the corresponding power at the surface. In contrast

**Table 3**
Operating parameters of experimental set-up A with brass and stainless-steel bolts.

| Designation | Unit | Experimental set-up A |
|---|---|---|
| Heat flux $\dot{q}$ | [W/cm$^2$] | 2.2 |
| Surface temperature $T_s$ | [°C] | 81 |
| Fluid temperature$T_{fl}$ | [°C] | 58 |
| Test series with brass bolts | | |
| Leckage current $I_{a,1}$ (TS1) | [mA] | 0 |
| Leckage current $I_{a,2}$ (TS2) | [mA] | 7 |
| Leckage current $I_{a,3}$ (TS3) | [mA] | 37 |
| Leckage current $I_{a,4}$ (TS4) | [mA] | 74 |
| Leckage current $I_{a,5}$ (TS5) | [mA] | 98 |
| Test series with stainless-steel bolts | | |
| Leckage current $I_{a,6}$ (TS6) | [mA] | 0 |
| Leckage current $I_{a,7}$ (TS7) | [mA] | 7 |
| Leckage current $I_{a,8}$ (TS8) | [mA] | 37 |
| Leckage current $I_{a,9}$ (TS9) | [mA] | 74 |
| Leckage current $I_{a,10}$ (TS10) | [mA] | 98 |

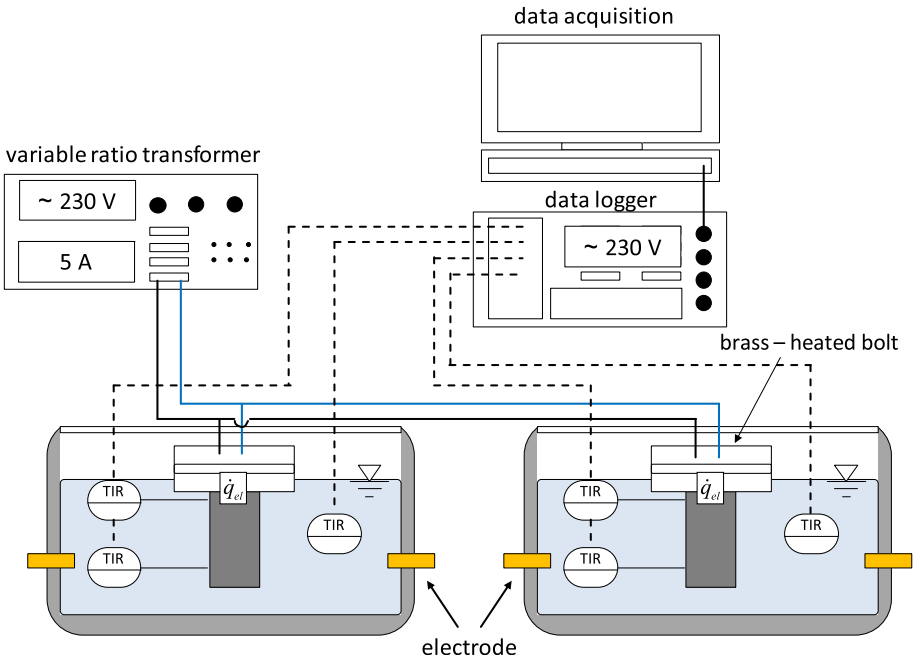


**Fig. 4.** Schematic of experimental set-up A.

to the investigations of Höfling [13] and Mayer [22], we used no stirrer, in order to achieve a visible effect of sedimentation and secondary crystallization.

Unlike the set-up A, experimental set-up B (see Fig. 5) was hydraulically connected in series. In this case, the inlet and outlet temperature and the flow rate were monitored. The flow control was adjusted by a variable differential pressure switch with an integrated diaphragm and a Venturi nozzle. The flow detection was monitored by the tankless water heater. The tankless water heater was used to generate a constant feed temperature. Furthermore, the absolute pressure at the inlet and outlet, the electrical conductivity and pH value were also recorded. In the series of tests with electrical leakage currents, the applied electrical voltage and the electrical current between the inlet and outlet were monitored, too.

Table 4 summarizes different test series of experimental set-up B.

## 3. Results and discussion

### 3.1. General influence of crystallization fouling in water heating

#### 3.1.1. Reproducibility of saturation index

In the following, the reproducibility of the thermal fouling resistance is analyzed and discussed. Reproducible measurements are difficult to realize because of continuous fluctuations in tap water quality. Fig. 6 shows three exemplary fouling curves, which were recorded with

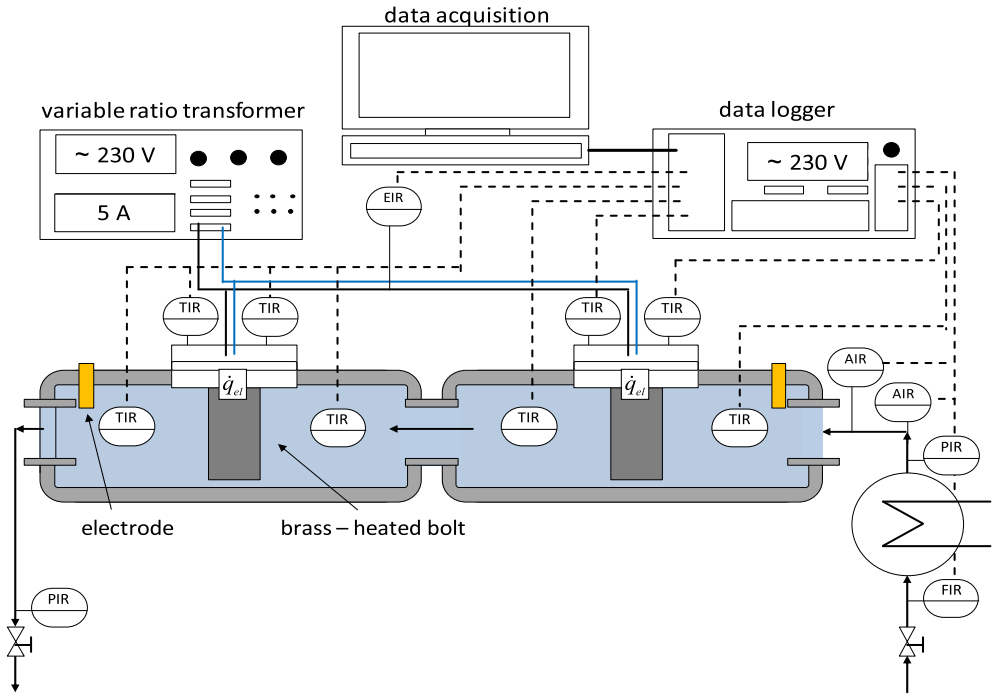


**Fig. 5.** Schematic of experimental set-up B.

**Table 4**
Parameters of test series of experimental set-up B.

| Tests (NE) | Heat flux $\dot{q}$ [W/cm$^2$] | Surface temp. $T_s$ [°C] | Liquid temp. $T_{fl}$ [°C] | Flow rate $\dot{V}$ [l/min] | Reynolds number = Re [-] | pressure $p_t$ [bar] | Leakage current $I_a$ [mA] | Saturation index SI [-] |
|---|---|---|---|---|---|---|---|---|
| 1 | 3.9 | 83 | 45 | 3 | 3950 | 1 | 0 | 0.85 |
| 2 | 3.9 | 85 | 45 | 3 | 3950 | 1 | 0 | 0.96 |
| 3 | 3.9 | 86 | 45 | 3 | 3950 | 1 | 0 | 0.97 |
| 4 | 5.6 | 80 | 30 | 3 | 3950 | 1 | 0 | 0.67 |
| 5 | 3.1 | 89 | 60 | 3 | 3950 | 1 | 0 | 1.11 |
| 6 | 2.9 | 73 | 45 | 3 | 3950 | 1 | 0 | 0.72 |
| 7 | 1.9 | 61 | 45 | 3 | 3950 | 1 | 0 | 0.52 |
| 8 | 3.5 | 89 | 45 | 2 | 2631 | 1 | 0 | 1.09 |
| 9 | 4.3 | 84 | 45 | 4 | 5263 | 1 | 0 | 1.01 |
| 10 | 3.9 | 77 | 45 | 3 | 3950 | 1 | 6 | 0.82 |
| 11 | 3.9 | 83 | 45 | 3 | 3950 | 1 | 16 | 0.87 |

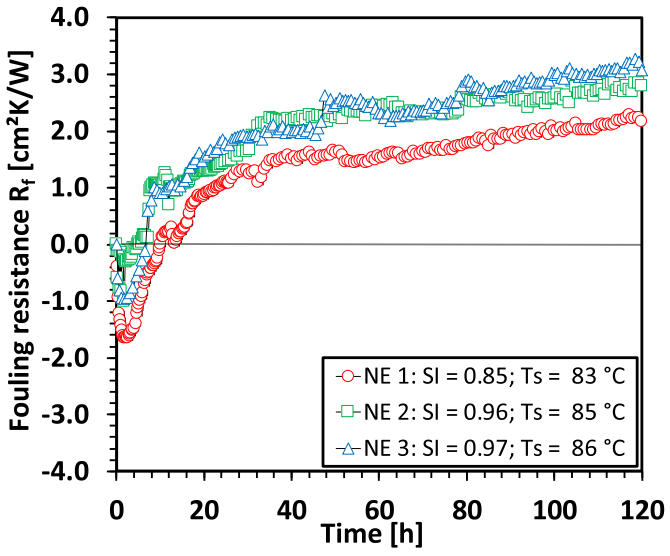


**Fig. 6.** Effect of fouling resistance with different saturation indexes (Set-up B; Re = 3950).

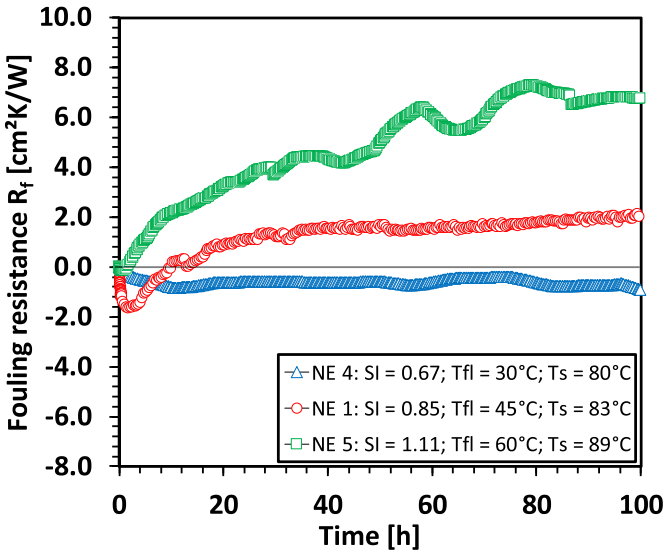


**Fig. 7.** Effect of liquid temperature on the fouling curve (Set-up B; Re = 3950).

identical settings over a period of more than six months. The only varied parameter in this case is the saturation index.

Basically, the thermal fouling behavior is similar over the measured period. At similar saturation indexes, as those measured in test series NE2 and NE3, the fouling curves are superimposed, and the deviation is in the range of 10%, which is considered acceptable for practical applications. In the study on the reproducibility of the induction time, Geddert [11] found a relative deviation of 10%–35% with constant saturation indexes and operating conditions. When the saturation indexes differ, the fouling resistance behavior and induction time are different, as can be seen with the test series NE1.

### 3.1.2. *Liquid temperature*

Fig. 7 demonstrates a significant dependence of the fouling resistance on the liquid temperature. The fouling curve in test series NE1 shows a well-defined, roughness-controlled induction period. After the induction period, a reduction in the deposition rate can be seen.

A reduction of the liquid temperature by 15 K in the test series NE4 leads to the blue fouling curve in Fig. 7. Although the saturation index was greater than zero, no crystal layer growth was detected. The roughness-controlled phase is initially dominated by the formation of the first nucleus and crystals. Subsequently, a negative fouling resistance is established. The conditions at the surface remain constant due to the increased heat transfer coefficient. There is no further increase in nucleus and crystal growth.

However, in the test series NE5 with the liquid temperature of 60 °C, the relationship is obviously nonlinear, and an induction phase can be observed. The roughness-controlled phase is driven exclusively by the dominant heat conduction resistance. In the subsequent layer growth stage, an asymptotic fouling behavior is observed, which evolves into a kind of saw tooth curve at a later time.

These results show that a change in the temperature level has a significantly higher impact on the fouling behavior than an increase in the saturation index, investigated in the previous test series.

### 3.1.3. *Surface temperature*

Fig. 8 illustrates the influence of the surface temperature on the fouling resistance.

It can be seen that the roughness-controlled phase becomes substantially shorter with smaller peaks, when the surface temperature increases. Additionally, the induction phase does not reveal any initialization period. Initially, nucleuses are formed, and crystal growth begins. This leads to an earlier enhancement of the heat transfer coefficient, which quickly reverts again because of the increasing heat conduction resistance. Consequently, as visible for test series NE6 and NE7, the linear development of crystal growth begins during the induction phase. This results in a considerable extension of the induction time. Furthermore, at test series NE7, a saw tooth course is detected in the layer growth phase. In addition, a temperature increases of 12K, visible in test series NE7 to NE6, does not influence the fouling behavior significantly.

### 3.1.4. *Flow rate*

Fig. 9 illustrates the influence of different flow rates on the fouling resistance.

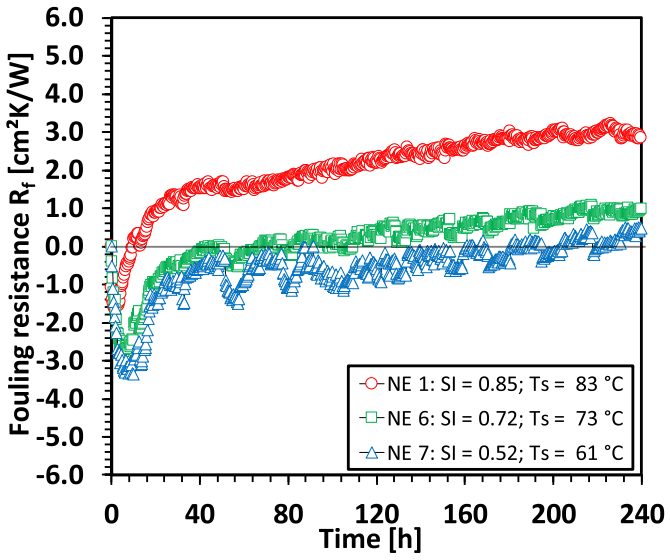


**Fig. 8.** Effect of surface temperature on the fouling curve (Set-up B; Re = 3950).

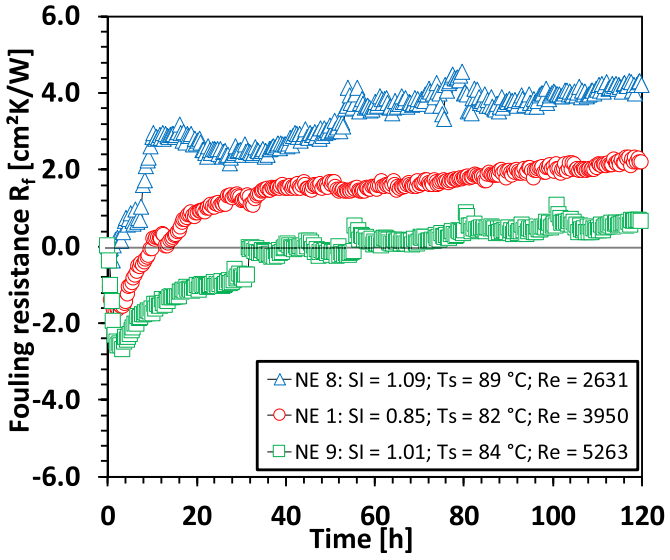


**Fig. 9.** Effect of flow rate on the fouling curve (Set-up B).

A reduction in the thermal fouling resistance and in the induction time with increasing flow rate was detected. This was induced by small crystals growing on the heat transfer surface and increasing turbulence. The latter led to an enhancement of the heat transfer coefficient. Furthermore, the effect of increasing fluid velocity caused two further improvements, namely, enhanced removal forces and inhibited growth of crystals on the heat transfer surface. Similar experimental results were also obtained and discussed by Geddert [11], Höfling [13] and Rizzo [18].

### 3.2. *Special influence of crystallization fouling in electric water heating*

In the following, the focus is on the influence of electrical leakage currents on the crystallization fouling. Since conventional bare-wire heating elements have a direct contact with the fluid, an electrical leakage current arises.

#### 3.2.1. *Influence of leakage current on the fouling resistance*

The fouling curves in Fig. 10 show that a defined AC electrical current is established if an AC voltage is applied.

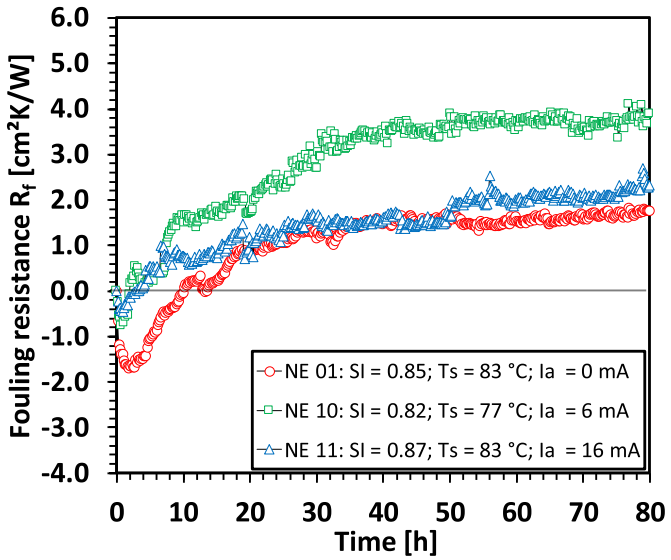


**Fig. 10.** Effect of leakage current on the fouling curve (Set-up B; Re = 3950).

The induction time is significantly reduced when the electrical current is increased, as shown in test series NE10 and NE11. Although the saturation index does not change in a reasonable way, the fouling curves are influenced by the leakage current. After completion of the test series, the inspection of the brass bolts show that the formation of the oxidation layer is partially hindered, as illustrated in Fig. 11.

Depending on the intensity and local orientation of the electric field at the brass bolt, partial oxidation is prevented, nucleation occurs at the oxidation-free surface, and the crystalline deposit on this clean surface begins. If this natural formation of the oxidation layer is prevented by the electric field caused by the applied voltage, stronger nucleation and crystal growth can take place than with the oxidation layer.

Considering the test series NE10 with a 6mA leakage current, the reasons for stronger influence in the growth layer phase are not obvious at first. Optical examination of the bolts after the tests showed that the electric field could not develop properly. Large parts of the bolt were not oxidized.

At test series NE11 with a leakage current of 16 mA, however, the electric field was well formed. It was obvious that a blank, oxide-free spot had formed in a direction of 90° relative to the flow of the electrical current, as shown in Fig. 11. The remaining bolt was provided with a pronounced oxidation layer. This means that the electrical leakage current has an influence on the local oxidation of the heat transfer surface and thus on the formation of the local nucleus sites, the induction time and fouling behavior.

Fig. 12 shows the dependence of the induction time on the electrical leakage current. The induction time is significantly reduced when the electrical current is increased.

#### 3.2.2. *Influence of leakage current on morphology*

This test series was primarily used to confirm that the crystal morphology is influenced by the electrical leakage current. Experimental set-up A was used for these investigations. Furthermore, not only brass bolts (CW 614 N) but also stainless-steel bolts (1.4301) were used.

Fig. 13 shows the contaminated brass bolt and the light microscope images of the brass bolt surface depending on the leakage current. Furthermore, IR spectra of deposited crystals are given for each tested brass bolt.

With increasing of electrical leakage current, the oxidation of the brass bolt increases and a defined oxide-free spot forms in a direction orthogonal to the electrical current flow, just as with the test series in the previous section. The oxide-free spot is more affected than the oxidized surface. In the study with oxidized surfaces, Rizzo [18] found a direct

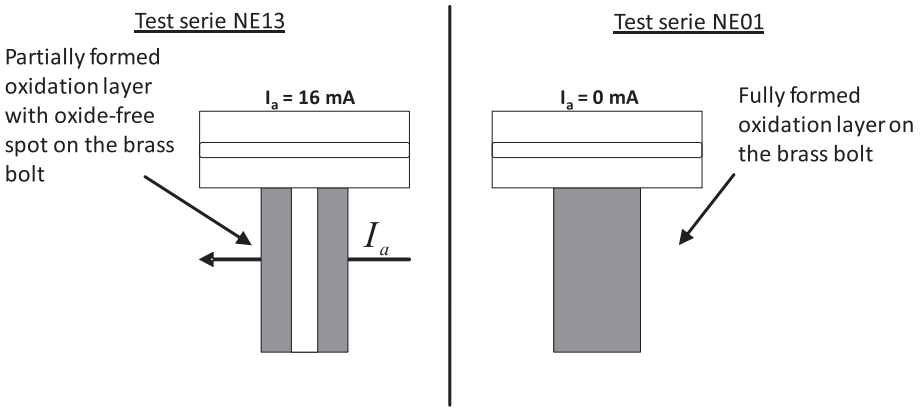


**Fig. 11.** Schematic representation of the optical observations of the brass bolt in test series NE01 (right) and NE13 (left).

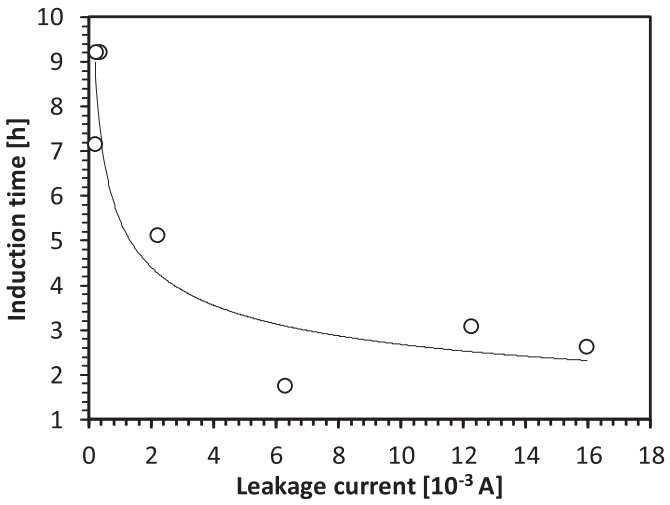


**Fig. 12.** The relationship between the leakage current and induction time.

dependence between the degree of oxidation and oxidation depth. In the present investigations, an increase in the degree of oxidation was observed with rising electrical leakage current. In addition, an increase in crystal populations per unit area was also seen with increasing electrical leakage current.

Furthermore, IR spectra of deposited crystals on each brass bolt are presented in Fig. 13. It can be seen that the characteristic wave numbers (black numbers) at 1783 $cm^{-1}$, 1483 $cm^{-1}$, 1082 $cm^{-1}$, 859 $cm^{-1}$, 712 $cm^{-1}$ and 699 $cm^{-1}$ prove the presence of calcium carbonate in the crystal-form aragonite in all test series TS1 to TS5 [23]. Moreover, the IR spectra at test series TS3 to TS5 show that additional wave numbers (red numbers) at 1630 $cm^{-1}$, 1166 $cm^{-1}$, 1110 $cm^{-1}$ and 612 $cm^{-1}$ appeared. This fact reveals that the deposition on the brass bolts exhibits the presence of a crystal mixture based on aragonite in test series TS3 to TS5. Small valleys of these additional wave numbers at 1630 $cm^{-1}$, 1166 $cm^{-1}$, 1110 $cm^{-1}$ and 612 $cm^{-1}$ indicate that it is present in negligible quantity thus making identification difficult. Furthermore, a slight dezincification may have occurred on the brass bolts. Greenish brash oxide was not visible in these test series unlike in Teng et al. [24]. In the images of the brass bolt (Fig. 13), it is visible that a slight reddish surface coloration has developed. This could be an indication that dezincing begins. If this phenomenon occurs, the heating surface is changed, and stronger nucleation and crystal growth can take place. With this in mind, it could be possible that the additional wave numbers show the presence of zinc sulfate ($ZnSO_4{\cdot}7H_2O$) with the characteristic wave numbers at 1640 $cm^{-1}$, 1100 $cm^{-1}$, 990 $cm^{-1}$, 725 $cm^{-1}$ and 612 $cm^{-1}$ [25], which means a further indication of dezincification.

The contaminated surface was further analyzed by X-ray fluorescence analysis. The results are shown in Table 5. The X-ray fluorescence spectrum without crystals shows an increase of lead contents with increasing leakage current. This also could be an indication of dezincification.

In the test series with stainless-steel bolts, similar results were found as in the test series with brass bolts, as shown in Fig. 14. With increasing electrical leakage current, an increase in crystal populations per unit area was also observed. The IR spectra showed the characteristic wave numbers of calcium carbonate in the modification phase aragonite in all test series, too. Note that only crystal deposition formed and no clear corrosion effects were observed on stainless-steel surface after the fouling tests with different AC leakage current. Table 6 shows the results of the X-ray fluorescence analysis.

IR spectra of deposited crystals at test series TS9 to TS10 show that additional wave numbers at 1630 $cm^{-1}$, 1065 $cm^{-1}$, 999 $cm^{-1}$,612 $cm^{-1}$,550 $cm^{-1}$ and 456 $cm^{-1}$ can be detected. These wave numbers are different from the wave number of the crystal deposition on the brass bolt surface. On the one hand, the present crystal mixture could be a compound of iron sulfate ($FeSO_4{\cdot}7H_2O$) with the characteristic wave numbers at 1630 $cm^{-1}$, 1350 $cm^{-1}$, 1100 $cm^{-1}$, 990 $cm^{-1}$, 720 $cm^{-1}$, 612 $cm^{-1}$, 550 $cm^{-1}$and 450 $cm^{-1}$ [25], which shows the tendency to corrosion effects. On the other hand, these additional crystals could be magnesium hydroxide with the characteristic wave numbers at 1630 $cm^{-1}$, 1065 $cm^{-1}$, 1000 $cm^{-1}$, 640 $cm^{-1}$, 575 $cm^{-1}$ and 465 $cm^{-1}$ [26]. A clear identification, what is really formed, is difficult. However, it becomes clear that the deposited crystals on stainless-steel bolts exhibits the presence of crystal mixture based on aragonite in test series TS9 to TS10.

Furthermore, a decrease in crystal length and a reduction of the hydraulic crystal diameter with rising electrical leakage current was found, too.

Fig. 15 illustrates the relationship between the crystal length and crystal diameter and the electrical leakage current.

The present investigations show that the electrical leakage current has a direct influence on crystallization fouling. On the one hand, local oxidation is promoted by the electrical leakage current (anodic oxidation development); at the same time, however, it is also prevented on the surface (cathodic oxidation reduction). On the other hand, rising electrical leakage current increases the nucleation population and crystallization density per area.

### 3.3. *Processing of the experimental data*

According to Bohnet [27] and Karpinski [28], the crystal growth phase is divided into two consecutive steps. The dissolved ions are first transported by convection or diffusion from the bulk flow through the diffusion and adsorption boundary layer to the phase boundary. After a chemical reaction, the ions are incorporated into the existing crystals.

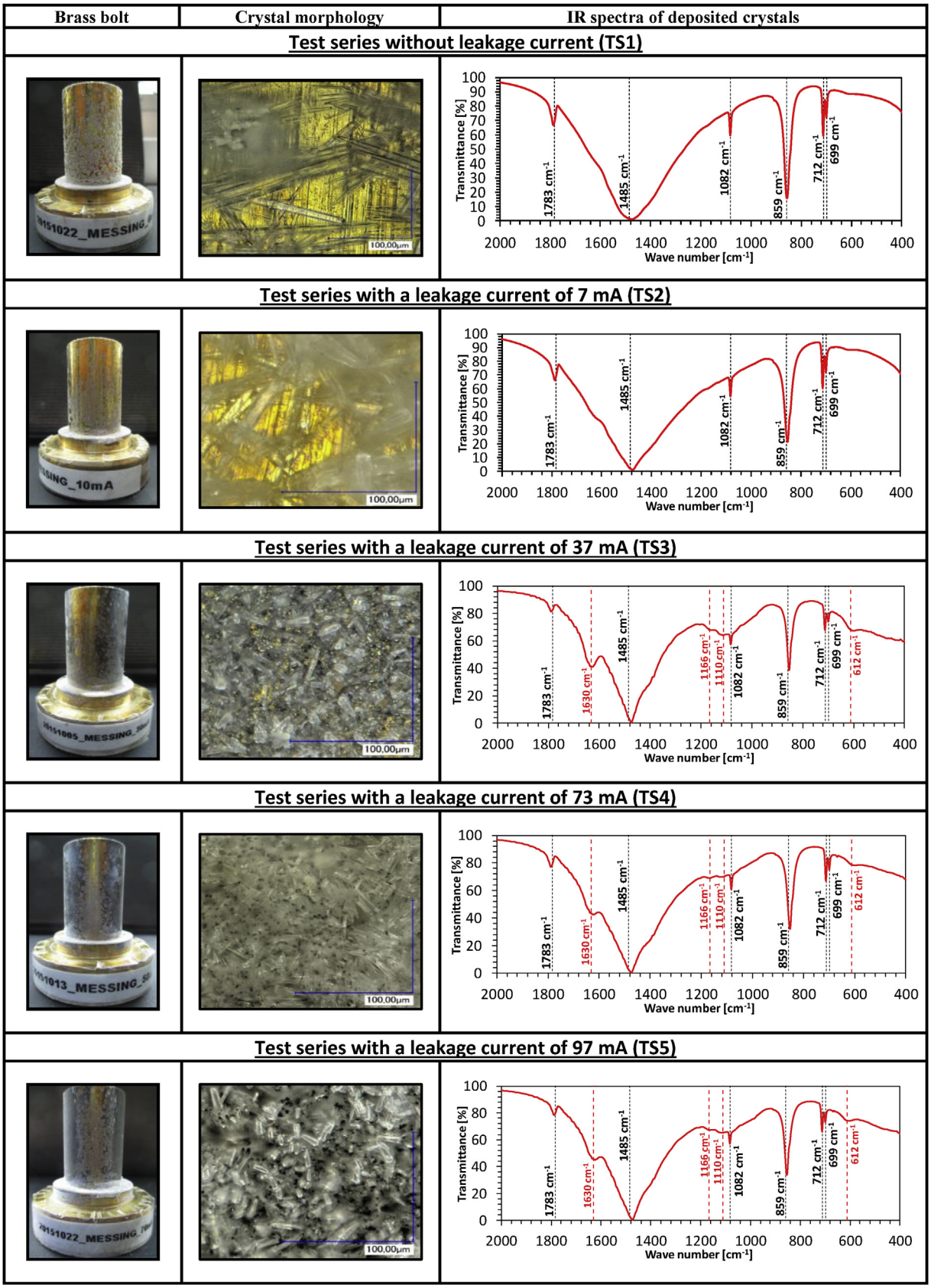


**Fig. 13.** Contaminated brass bolt, crystal morphology and IR spectra of deposited crystals in dependence on the leakage current.

**Table 5**
Results of X-ray fluorescence analysis on brass bolts without deposited crystals.

| Test- | $I_a$ [mA] | Cu [%] | Sn [%] | Pb [%] | Zn [%] | Fe [%] | Ni [%] | Mn [%] | Other [%] |
|---|---|---|---|---|---|---|---|---|---|
| TS1 | 0 | 57.93 | 0.27 | 2.86 | 38.35 | 0.28 | 0.08 | 0.08 | 0.1 |
| TS2 | 7 | 58.24 | 0.29 | 2.94 | 37.91 | 0.24 | 0.07 | 0.10 | 0.2 |
| TS3 | 37 | 54.89 | 0.62 | 3.88 | 39.33 | 0.39 | 0.11 | 0.14 | 0.6 |
| TS4 | 73 | 55.63 | 0.84 | 4.73 | 37.08 | 0.39 | 0.11 | 0.21 | 1.0 |
| TS5 | 97 | 54.72 | 1.16 | 5.29 | 36.43 | 0.52 | 0.14 | 0.29 | 1.5 |

The mass transfer by convection and diffusion can be represented as follows:

$$J_{i,D} = \frac{\dot{m}_{i,D}}{A_{HTS}} = \beta \cdot (\rho_F - \rho_{ad}) \tag{11}$$

In Eq. (11) is $\dot{m}_{i,D}$ the deposition mass flow rate and $A_{HTS}$ is the heat transfer surface. Furthermore, $\beta$ is the mass transfer coefficient and $\Delta\rho_{Fad}=(\rho_F-\rho_{ad})$ is the mass concentration difference between the fluid and the adsorpion boundary layer.

The incorporation reaction of the salt ions into the existing crystal structure can be described by the following reaction kinetics (Eq. (12)), in which $k_R$ is the reaction rate constant and $\Delta\rho_{ads}=(\rho_{ad}-\rho_s)$ is the mass concentration difference between the adsorpion boundary layer and the heating surface:

$$J_{i,D} = \frac{\dot{m}_{i,D}}{A_{HTS}} = k_R \cdot (\rho_{ad} - \rho_s)^q \tag{12}$$

According to Müller-Steinhagen [6], the exponent $q$ defines the reaction order and can be assumed to be 2 for the substance system $CaCO_3$. From Eqs. (11) and (12), the following expression follows:

$$J_{i,D} = \frac{\dot{m}_{i,D}}{A_{HTS}} = \beta \cdot \left[ \frac{1}{2} \cdot \left( \frac{\beta}{k_R} \right) + (\rho_F - \rho_s) - \left( \frac{1}{4} \cdot \left( \frac{\beta}{k_R} \right)^2 + \left( \frac{\beta}{k_R} \right) \cdot (\rho_F - \rho_s) \right)^{\frac{1}{2}} \right] \tag{13}$$

The deposition mass flux $J_{i,D}$ can now be determined as a function of the concentration difference $\Delta\rho_{Fs}=(\rho_F-\rho_s)$. However, Eq. (13) does not take into account the influence of the electrical leakage current. This requires a derivation of a relationship from the Nernst-Planck equation [16], which subdivides the entire deposition mass flux $J_{i,MD}$ into two partial mass fluxes. First part is the electro migration mass flux $J_{i,M}$ and second part is the diffusion mass flux $J_{i,D}$ (see Eq. (14)):

$$J_{i,MD} = J_{i,M} + J_{i,D} \tag{14}$$

The determination of the migration mass flux $J_{i,M}$ as a function of the electrical potential difference can be described by the following Eq. (15), in which $\widetilde{M}_i$ is the molar mass, $c_i$ is the molar concentration, $z_i$ is the ion value, $F$ is the Faraday constant, $\Re$ is the Universal gas constant and $\Delta\varphi=(\varphi_s - \varphi_F)$ is the electrical potential difference between the heating surface and the fluid.

$$J_{i,M} = \frac{\widetilde{M}_i \cdot c_i \cdot z_i \cdot F \cdot \beta}{\Re \cdot T} \cdot (\varphi_s - \varphi_F) \tag{15}$$

The electro migration mass flux $J_{i,M}$ can contribute significantly to the overall mass transport only if the electrical potential difference $\Delta\varphi=(\varphi_s - \varphi_F)$ is sufficiently large. According to Hamann and Vielstich [16], this is not the case in most practical applications. In the application range of electric water heating, however, the effect of the electrical potential difference is significant. Adding the two partial mass fluxes (Eq. (13) and Eq. (15)) into Eq. (14) yields the following relationship:

$$J_{i,MD} = \beta \cdot \left[ \frac{\widetilde{M}_i \cdot c_i \cdot z_i \cdot F}{\Re \cdot T} \cdot \Delta\varphi + \frac{1}{2} \cdot \left( \frac{\beta}{k_R} \right) + (\rho_F - \rho_s) - \left( \frac{1}{4} \cdot \left( \frac{\beta}{k_R} \right)^2 + \left( \frac{\beta}{k_R} \right) \cdot (\rho_F - \rho_s) \right)^{\frac{1}{2}} \right] \tag{16}$$

In the tests performed, a strong oxidation layer formed on the heat transfer surface of the brass bolts. In order to take this fact into account, the so-called oxidation factor $f_{OT}$ is introduced, and the deposition mass flux $J_{i,MD}$ is multiplied by this factor:

$$J_{i,MD,f} = J_{i,MD} \cdot f_{OT} \tag{17}$$

Based on our experimental results and on the experimental investigations of Rizzo [18], the following equation is derived:

$$f_{OT} = -1.6406 \cdot \phi + 2.1274 \tag{18}$$

The oxidation factor is used to estimate the influence of local oxidation on the brass bolt. If the surface under consideration is completely covered by the oxidation layer (degree of oxidation coverage $\phi = 1$), the fouling mass flux is reduced by almost 50%. If the degree of coverage decreases, the fouling mass flux increases correspondingly.

The mass transfer coefficient $\beta$ required for the calculation of the deposition mass flux $J_{i,MD}$was determined from the heat and mass transfer analogy with the following Sherwood number $Sh$ correlation for pipe flows according to Gnielinski [29]:

$$Sh = \frac{\left(\frac{\xi}{8}\right) \cdot (Re - 1000) \cdot Sc}{1 + 12.7 \cdot \left(\frac{\xi}{8}\right)^{0.5} \cdot (Sc^{0.66} - 1)} \cdot \left( 1 + \left( \frac{d_c}{L} \right)^{\frac{2}{3}} \right) \tag{19}$$

where $\xi$ is the coefficient of friction, $Re$ is the Reynolds number, $Sc$ is the Schmidt number, $d_c$ is the characteristic pipe diameter and $L$ is the pipe length.

Subsequently, the mass transfer coefficients $\beta$ were determined according to the recommendation of Müller-Steinhagen [6]:

$$\beta = f_{BB} \cdot Sh \cdot \frac{D_T}{d_c} \tag{20}$$

$$D_T = D_{CaCO_3} \cdot \frac{T_{fl}}{T_{R,C}} \cdot \exp\left( 3.8 \cdot T_{fl} \cdot \left( \frac{1}{T_{R,C}} - \frac{1}{T_{fl}} \right) \right) \tag{21}$$

$$D_{CaCO_3} = 1.14563 \cdot 10^{-9} \ m^2/s \quad \text{(at 336 K)}$$

In Eqs. (20) and (21), $D_T$ is the extrapolated diffusion coefficient, $D_{CaCO_3}$ is the diffusion coefficient for calcium carbonate at a temperature $T_{R,C}$ of 336 K.

It should be noted that the correction factor $f_{BB}$ is introduced for the determination of the mass transfer coefficient considering the bolt geometry. Fig. 16 illustrates the relationship between the Sherwood number $Sh$ and the correction factor $f_{BB}$.

Najibi et al. [30] observed that the reaction rate constant $k_R$ increases exponentially with the absolute temperature and therefore suggested its

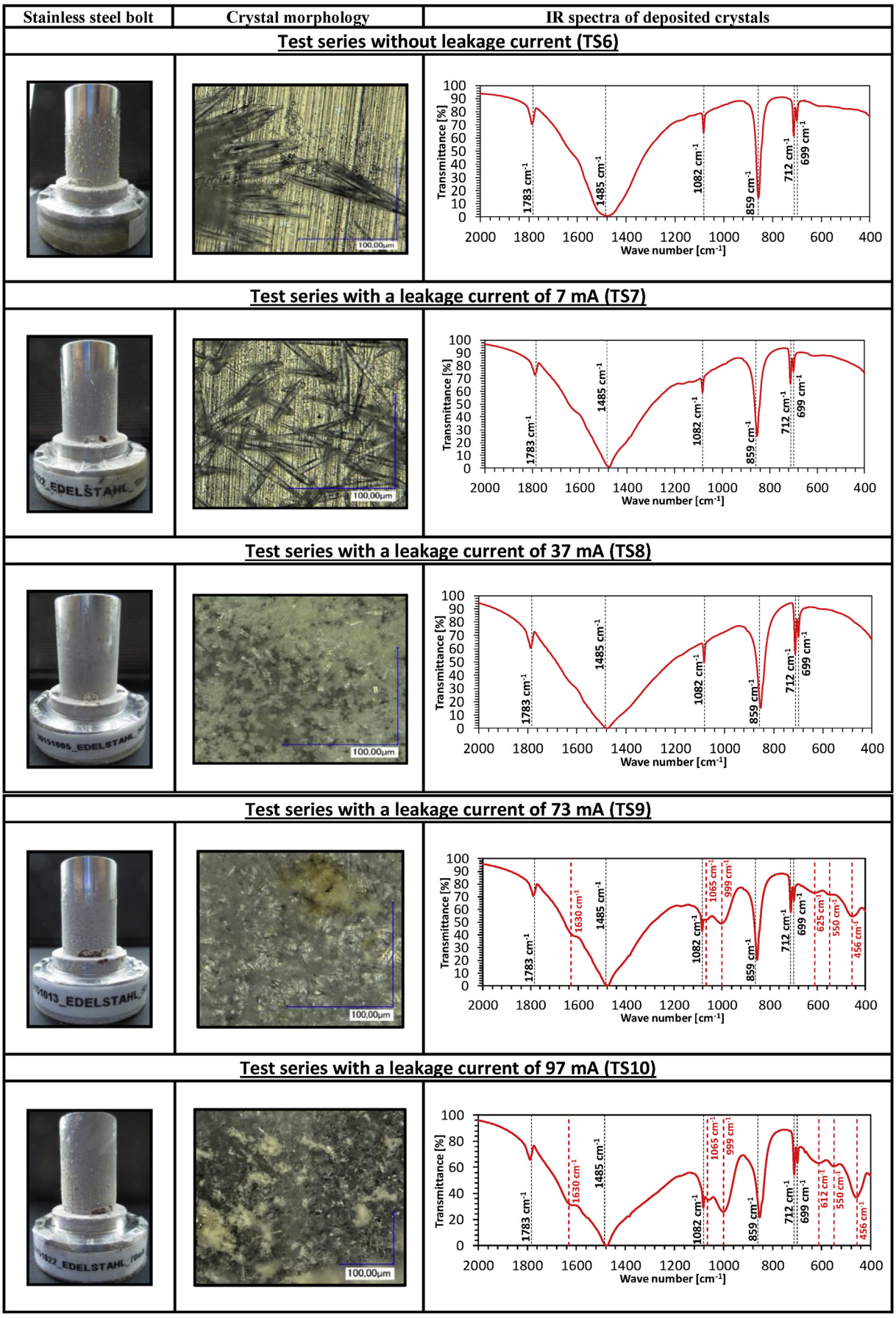


**Fig. 14.** Contaminated stainless-steel bolt, crystal morphology and IR spectra of deposited crystals in dependence on the leakage current.

**Table 6**
Results of X-ray fluorescence analysis on stainless-steel bolts without deposited crystals.

| Test | $I_a$ [mA] | Fe [%] | Ni [%] | Cr [%] | Mo [%] | Nb [%] | Cu [%] | Mn [%] | Other [%] |
|---|---|---|---|---|---|---|---|---|---|
| TS6 | 0 | 71.27 | 8.13 | 18.53 | 0.28 | 0.01 | 0.49 | 1.01 | 0.3 |
| TS7 | 7 | 70.94 | 8.41 | 18.05 | 0.35 | 0.03 | 0.66 | 0.78 | 0.8 |
| TS8 | 37 | 71.18 | 8.22 | 18.51 | 0.28 | 0.01 | 0.50 | 1.04 | 0.3 |
| TS9 | 73 | 71.97 | 7.82 | 18.19 | 0.27 | 0.00 | 0.46 | 1.06 | 0.2 |
| TS10 | 97 | 71.28 | 8.18 | 18.48 | 0.28 | 0.01 | 0.51 | 1.00 | 0.3 |

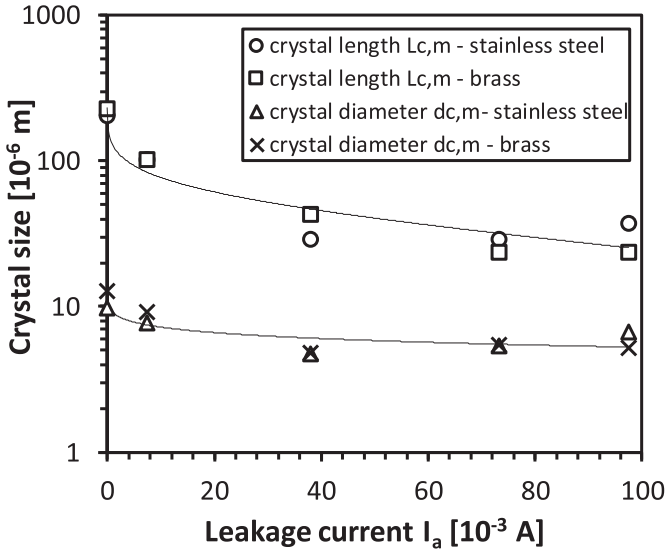


**Fig. 15.** Correlation between crystal size and leakage current.

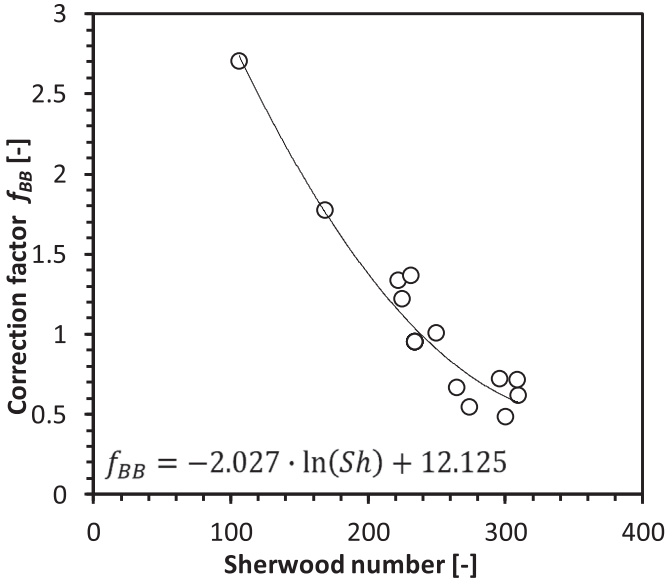


**Fig. 16.** Correlation between Sherwood number and correction factor $f_{BB}$.

estimation with an Arrhenius approach. The activation energy $E$ and reaction constant $k_{1,0}$ for $CaCO_3$ can be taken from Müller-Steinhagen [6].

$$k_R = k_{1,0} \cdot \exp\left(-\frac{E}{\Re \cdot T_s}\right) \tag{22}$$

In order to estimate the partial mass flux $J_{i,M}$ from Eq. (15) as a function of the electrical potential difference, the following procedure is proposed. As explained above, there is an electrical potential difference between the heat transferring metallic surface and the fluid. During the investigations, a defined alternating voltage difference $\Delta\varphi_{AC}$ is superimposed on this natural potential difference $\Delta\varphi_{DC}$. This results in a mixed potential, which can be determined by the following equation:

$$\Delta\varphi = \sqrt{\Delta\varphi_{DC}^2 + \Delta\varphi_{AC}^2} \tag{23}$$

The voltage in experimental set-up B is measured across the electrodes in all test series, including experiments in which no external voltage is applied. In this case, a DC voltage is measured. The average DC electrical potential difference $\Delta\varphi_{DC}$ is 0.9V across the experimental set-up. By assuming a series connection of ohmic resistors for the different test components of the test sections, it can be supposed that the electrical current has the same order of magnitude at every point. Thus, if the diffusion boundary layer thickness $\delta_{DL}=D_T/\beta$ is known, the potential difference between the bolt and fluid at a direct current $I_{DC}$ is to be calculated as follows:

$$\Delta\varphi_{DC} = I_{DC} \cdot \left[\frac{\rho_{Me} \cdot d_{BB}}{A_{q,BB}} + \frac{\rho_F \cdot \delta_{DL}}{A_{q,F}}\right] \tag{24}$$

where $\rho_{Me}$ is the electrical resistivity of the used bolt and $\rho_F$ is the electrical resistivity of the fluid, $d_{BB}$ is the diameter of the bold, $A_{q,BB}$ is the cross-sectional area of the bolt and $A_{q,F}$ is the cross-sectional area of the fluid.

In a similar way, the potential drop is also determined in the case of an alternating current $I_{AC}$.

$$\Delta\varphi_{AC} = I_{AC} \cdot \left[\frac{\rho_{Me} \cdot d_{BB}}{A_{q,BB}} + \frac{\rho_F \cdot \delta_{DL}}{A_{q,F}}\right] \tag{25}$$

The crystallization fouling is often superimposed by the layer growth and layer removal stages in the surrounding heating surfaces. According to Kern et al. [31], the fouling mass flux $J_f$ can be formulated by balancing the two mass fluxes, one for deposition, $J_{i,MD,f}$, and another for removal, $J_r$. The influence of the layer removal on the crystallization fouling is analyzed by Förster [10], Bohnet [27] and Hirsch [32]. According to Förster [10], the fouling mass flux $J_f$ can be described as follows:

$$J_f = J_{i,MD,f} - J_r = J_{i,MD,f} \cdot \left[1 - \Gamma\left(\frac{F_\tau}{F_H}\right)\right] \tag{26}$$

Förster [10] formulates the removal term with the aid of the removal probability $\Gamma$. The latter is dependent on the ratio between the fluid shear forces $F_\tau$ and adhesion forces $F_H$. In addition, the Weibull distribution is used to take into account the fracture mechanics of the brittle crystalline deposits. The determination of the removal probability is given elsewhere (see Refs. [10] or [33]).

The removal probability $\Gamma$ determined in our investigations is shown in Fig. 17.

The proposed calculation approach can be used to estimate the fouling mass with Eq. (27) at the end of the testing time $t_{end}$, assuming a linear fouling mass flux:

$$m_f = J_f \cdot A_{HTS} \cdot t_{end} \tag{27}$$

The fouling mass $m_f$ is determined after each experiment by means of the bolt weight increase.

The calculated fouling masses deviate from the measured values by ± 30% (see Fig. 18). Above all, the deviations are significant for small

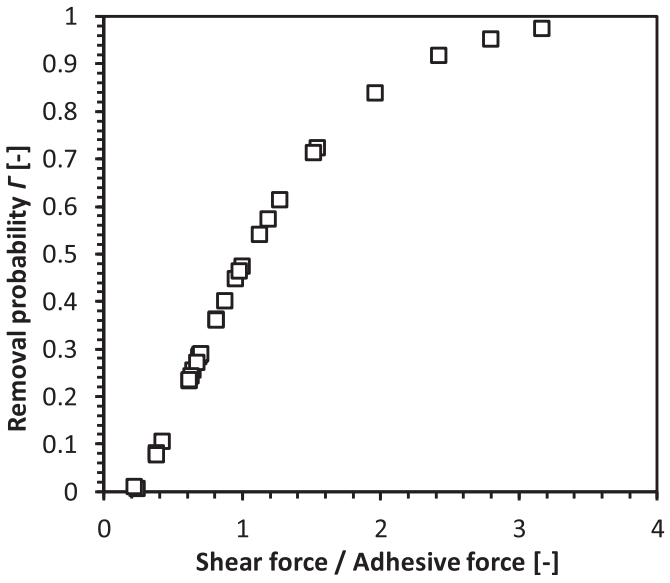


**Fig. 17.** Removal probability as a function of the force ratio.

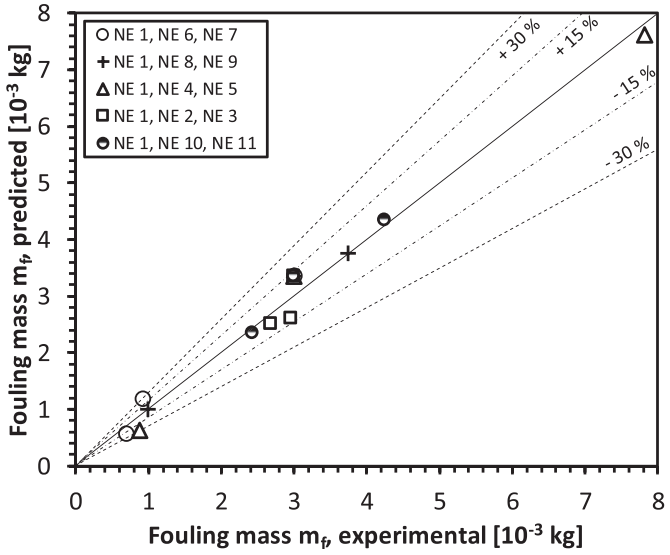


**Fig. 18.** Comparison of the experimental fouling mass $m_f$ and the prediction of our model.

deposits; they become smaller with increasing fouling mass. For a fouling mass over 2 grams, the deviations are less than ±15%.

## 4. Conclusions

The results of the present work show that the main factors influencing crystallization fouling in electric water heating are saturation index, liquid and surface temperature and flow rate. These characteristic variables basically influence the temporal development of the fouling resistance, as well as the turn point time and induction time. Furthermore, it was shown that the electrical leakage current also influences the fouling process. This means an influence on the local oxidation of the heat transfer surface of brass and thus on the formation of the local nucleus sites, on induction time and on fouling behavior. An increase in crystal populations per unit area with increasing electrical leakage current on brass and stainless-steel surfaces was also seen. Further observed effects were a decrease in crystal length and a reduction of the hydraulic crystal diameter with rising electrical leakage current. The IR spectra show that the deposition on the brass and stainless-steel bolts exhibits the presence of crystal mixture based on aragonite. Thus, with increasing leakage current the morphology of deposited crystals changes. Moreover, a slight dezincification may have occurred on the brass bolts during the fouling tests. This phenomenon could influence the heating surface and stronger nucleation and crystal growth can take place. On stainless-steel bolts, no clear corrosion effects were observed after the fouling tests. Correlations were derived, which took the influence of the electrical leakage current on the induction time and crystal size distribution into account. The relations between the fouling mass flux and the influencing factors can be properly captured by the proposed modeling approach. The model shows a reasonable prediction capacity, with deviations from experiments less than 15% for fouling deposits over 2 grams.

## Declarations

### *Author contribution statement*

Alexander Janzen, Eugeny Kenig: Conceived and designed the experiments; Performed the experiments; Analyzed and interpreted the data; Contributed reagents, materials, analysis tools or data; Wrote the paper.

### *Funding statement*

This research did not receive any specific grant from funding agencies in the public, commercial, or not-for-profit sectors.

### *Competing interest statement*

The authors declare no conflict of interest.

### *Additional information*

No additional information is available for this paper.

## References

[1] K.J. Brown, R. Farrelly, S.M. O'Shaughnessy, A.J. Robinson, Energy efficiency of electric infrared heating elements, Appl. Energy 162 (15 January 2016) 581–588.
[2] W. Rowlands, B. Vaidhyanathan, Additive manufacturing of barium titanate based ceramic heaters with positive temperature coefficient of resistance (PTCR), J. Eur. Ceram. Soc. 39 (12) (September 2019) 3475–3483.
[3] A. Raduta, M. Nicoara, R.L. Cucuruz, C. Locovei, Optimal Design of Heating Elements Sheathed with INCOLOY Superalloy 800, WSEAS Trans. Appl. Theor. Mech. 5 (3) (July 2010).
[4] G. Sureshkannan, M. Velliangiri, Raman analysis and experimental investigation of nichrome and aluminium nitride microtubular coil heaters: a 2D approach, Int. J. Mech. Eng. Robot. Res. 2 (2) (April 2013), 2278.
[5] L.O. Gusig, E. Schmitz, The Transient thermal Response of Conventional and New Ceramic Electrical Heating Elements under Forced Convection, Industrial Furnaces and Boilers. European Conference No 5, Espinho-Porto, Portugal, 2000.
[6] H. Steinhagen, Handbook of Heat Exchanger Fouling, IChemE, Warwickshire, UK, 2000.
[7] L.D. Tijing, H.Y. Kim, D.H. Lee, C.S. Kim, Y.I. Cho, Mitigation of Calcium Carbonate Fouling Using RF Electric fields, 2009 published online, www.heatexchanger-fouling.com. Austria.
[8] S. Krause, Fouling of heat-transfer surfaces by crystallization and sedimentation, Int. Chem. Eng. 33 (3) (1993).
[9] W. Augustin, Verkrustung (Fouling) von Wärmeübertragungsflächen, Dissertation; TU Braunschweig, 1993.
[10] M.L. Förster, Verminderung des Kristallisationsfoulings durch gezielte Beeinflussung der Grenzfläche zwischen Kristallen und Wärmeübertragungsflächen, Dissertation; TU Braunschweig, 2001.
[11] T. Geddert, Einfluss von Oberflächenmodifikationen auf die Induktionszeit beim Kristallisationsfouling, in: S. Scholl, W. Augustin (Eds.), ICTV – Schriftreihe Band 6, Cuvillier, Göttingen, 2009.
[12] F. Albert, Grenzflächeneffekte bei der kristallinen Belagbildung auf wärmeübertragenden Flächen, Dissertation, TU Braunschweig, 2010.
[13] V. Höfling, Kristallisationsfouling auf wärmeübertragenden Flächen durch Mehrkomponentensystem, Dissertation; TU Braunschweig, 2004.
[14] F. Wisotzky, Angewandte Grundwasserchemie, Hydrogeologie und hydrogeochemische Modellierung – Grundlagen, Anwendungen und Problemlösungen, Springer-Verlag Berlin, Heidelberg, 2011.

[15] T. Erdey-Grúz, Kinetik der Elektrodenprozesse, Akademia Kiado, Budapest, 1975.
[16] H.C. Hamann, A. Hamnett, W. Vielstich, Electrochemistry, Wiley-VCH Verlag GmbH & Co. KGaA, Weinheim, 2007.
[17] J.K. Vetter, Electrochemical Kinetics: Theoretical and Experimental Aspects, Academic Press, 1967.
[18] G. Rizzo, Induktionszeit Beim Kristallisationsfouling an Ionenimplantierten Wärmeübertragerflächen, Dissertation, Universität Stuttgart, 2008.
[19] E. Sarver, Y. Zhang, M. Edwards, Review of brass dezincification corrosion in potable water systems, Corros. Rev. 28 (3&4) (2010).
[20] A. Adebayo, B.S. Oluwadare, Corrosion of steels in water and hydrogen sulphide, Rev. Ind. Eng. Lett. 1 (2) (2014) 80–88.
[21] D. Parkhurst, C.A.J. Appelo, Description of Input and Examples for PHREEQC Version 3 – A Computer Program for Speciation, Batch-Reaction, One-Dimensional Transport, and Inverse Geochemical Calculations, U.S. Geological Survey Techniques and Methods, Book 6, Chap. A43, 2013, p. 497.
[22] M. Mayer, Modellierung der Mechanismen während der Induktionsphase beim Kristallisationsfouling, Dissertation, TU Braunschweig, 2013.
[23] V.N. Chukanov, Infrared Spectra of Mineral Species, Springer, Dordrecht, 2014.
[24] K.H. Teng, N.S. Kazi, A. Amiri, A.F. Habali, M.A. Bakar, B.T. Chew, A. Al-Shamma'a, A. Haw, K.H. Solangi, Ghulamulah Khan, Calcium carbonate fouling on double-pipe exchanger with different exchanging surfaces, Powder Technol. (2017).
[25] A.R. Nyquist, O. Kagel, Infrared Spectra of Inorganic Compounds, Academic Press, New York and London, 1971.
[26] H. Moenke, Mineral Spektren I, Akadem. Verl.-Ges. Geest & Portig (1962).
[27] M. Bohnet, Fouling of heat transfer surfaces, Chem. Eng. Technol. 10 (2) (1987) 113–125.
[28] P.H. Karpinski, Importance of the two-step crystal growth model, Chem. Eng. Sci. 40 (1985) 641–646.
[29] V. Gnielinski, Neue Gleichungen für den Wärme- und Stoffübergang in turbulent durchströmten Rohren und Kanälen, Forsch. Im. Ingenieurwes. 41 (1) (1975). S. 8-16.
[30] S. Najibi, H. Müller-Steinhagen, M. Jamialahmadi, Calcium Sulphate scale formation during subcooled flow boiling, Chem. Eng. Process., Bd. 20 (1986). S. 27-32.
[31] D.Q. Kern, R.E. Seaton, Theoretical analysis of thermal surface fouling, British Chem. Eng., Bd. 4 (1959). S. 258–262.
[32] H. Hirsch, W. Augustin, M. Bohnet, Influence of fouling layer shear strength on removal behaviour, in: T.R. Bott, et al. (Eds.), Understanding Heat Exchanger Fouling and its Mitigation, Begell House, New York, 1999, pp. 201–208.
[33] L. Sachs, Statistische Auswertungsmethoden, Springer-Verlag, Berlin, Heidelberg, New York, 1968.